



# Baseline-Free Damage Diagnostic Imaging Approach Relying on the Extraction of Converted Modes of Ultrasonic Guided Waves

Jiaqi Zhang<sup>1</sup>; Hao Xu<sup>2</sup>; Kai Zhou, Ph.D.<sup>3</sup>; Zhengyan Yang, Ph.D.<sup>4</sup>; Kehai Liu, Ph.D.<sup>5</sup>; Yuebin Zheng<sup>6</sup>; Shuyi Ma, Ph.D.<sup>7</sup>; and Zhanjun Wu<sup>8</sup>

**Abstract:** Large-scale plate-like structural components have been widely used in various aerospace structures. Subject to complex loading conditions and environmental factors, the integrity of plate-like structures is threatened by the occurrence and accumulation of structural damages, calling for the development of structural health monitoring (SHM) methods and techniques. Guided wave-based SHM methods have been demonstrated with a high sensitivity to small-scale damage. In particular, the probability-based diagnostic imaging (PDI) algorithm is able to achieve enhanced accuracy and efficiency of damage localization. Typically, the PDI defines damage index (DI) in terms of the deviation between the baseline and real-time guided wave signals. However, as the baseline signals are highly sensitive to environmental factors, such as temperature, the DI may exhibit large instability subject to varied environmental factors and lead to inaccurate damage detection results. In this study, a novel damage diagnostic imaging approach free of a baseline signal is presented for nonpenetrating damages. The approach is established based on the modification of conventional baseline-dependent PDI, into which the **converted mode extraction (CME)** strategy is integrated to give rise to the DI in terms of the energy of the converted modes. As the essential part of the CME-PDI approach, the converted modes caused by nonpenetrating damages as structural thickness variation are extracted from the primitive multimode wave signals according to a recently proposed CME method featured by intrinsic basis mode reconstruction. The effectiveness of the approach is first examined numerically, and then an experiment is carried out by taking into account the temperature effect. Compared with conventional PDI, the CME-PDI approach shows apparently enhanced accuracy and stability in damage localization. DOI: 10.1061/(ASCE)AS.1943-5525.0001319. © 2021 American Society of Civil Engineers.

**Author keywords:** Guided waves; Probability-based diagnostic imaging (PDI); Converted mode extraction (CME); Structural health monitoring (SHM); Damage identification.

## Introduction

In aerospace structures, the occurrence and accumulation of structural damage jeopardize the safety and integrity of in-service structures and may even result in catastrophic consequences (Xu et al. 2017). Thus, it is of vital importance to develop intelligent structures with self-sensing abilities, the essence of which resides in the development and integration of structural health monitoring (SHM) techniques (Bhalla and Soh 2004; Qing et al. 2007; Sohn et al. 2007). As ultrasonic guided waves in thin-walled structures exhibit unique advantages, including long propagation distance and high sensitivity to small damage (Su et al. 2006; Fan et al. 2015; Borate et al. 2020), guided wave-based SHM methods have been widely applied for rapid, long-range damage diagnosis in metallic and composite structures (Sohn et al. 2007; Yu et al. 2017; Qing et al. 2019). In recent years, guided wave-based damage diagnostic imaging techniques have attracted considerable preference because of their inherent capacity in **damage quantification**. In particular, the probability-based diagnostic imaging (PDI) method has been extensively studied (Wang et al. 2010; Zhou et al. 2011). **The main advantage of PDI is that the damage information can be directly extracted without tedious processing of signal features, such as the time of flight and group velocity.** Instead, correlation analysis along different propagation paths is sufficient to generate readily comprehensible images revealing the probability of damage locations

修改就在这里修改的

<sup>1</sup>Ph.D. Candidate, State Key Laboratory of Structural Analysis for Industrial Equipment, Dalian Univ. of Technology, Dalian 116024, China. ORCID: <https://orcid.org/0000-0002-2539-9164>. Email: zhangjq@mail.dlut.edu.cn

<sup>2</sup>Associate Professor, State Key Laboratory of Structural Analysis for Industrial Equipment, Dalian Univ. of Technology, Dalian 116024, China (corresponding author) Email: xuhao@dlut.edu.cn

<sup>3</sup>School of Urban Construction, Yangtze Univ., Jingzhou 434023, China. Email: zhoukai0513@163.com

<sup>4</sup>College of Transportation Engineering, Dalian Maritime Univ., Dalian 116024, China. Email: zyyang1993@dlmu.edu.cn

<sup>5</sup>Songshan Lake Materials Laboratory, Institute of Physics, Chinese Academy of Sciences, Guangdong 523808, China. Email: liukh@dlut.edu.cn

<sup>6</sup>Ph.D. Candidate, State Key Laboratory of Structural Analysis for Industrial Equipment, Dalian Univ. of Technology, Dalian 116024, China. Email: zhengyuebin@mail.dlut.edu.cn

<sup>7</sup>School of Traffic and Transportation, Dalian Univ. of Science and Technology, Dalian 116052, China. Email: dlut\_msy@163.com

<sup>8</sup>Professor, State Key Laboratory of Structural Analysis for Industrial Equipment, Dalian Univ. of Technology, Dalian 116024, China. Email: wuzhj@dlut.edu.cn

Note. This manuscript was submitted on October 28, 2020; approved on April 30, 2021; published online on July 20, 2021. Discussion period open until December 20, 2021; separate discussions must be submitted for individual papers. This paper is part of the *Journal of Aerospace Engineering*, © ASCE, ISSN 0893-1321.

(Gao et al. 2016). The damage index (DI) of PDI is usually calculated based on the deviation between the baseline data, collected under the **pristine** state of structures, and the real-time monitored data subject to damage occurrence (Qing et al. 2006a, b).

In spite of the proven effectiveness of PDI in many studies, baseline data is often difficult to obtain accurately. When subject to varied environmental factors, in particular, the propagation characteristics of guided waves would be greatly altered and are possible to result in false alarms and even failure of damage identification. Gorgin et al. (2020) provided a **state-of-the-art** review to discuss the influence of different factors (e.g., temperature and loading conditions) on guided wave propagation characteristics. Wang et al. (2014) attempted to suppress the impact of temperature and load on guided waves using adaptive filtering and the matching pursuit-based compensation (Wang et al. 2020). Efforts have also been made to eliminate the dependence on prior information of baseline data using methods, including cross-correlation analysis (Alem et al. 2016), similar path (Sun et al. 2019), the refined Lamb wave time-reversal method (Kannusamy et al. 2020), and so forth.

Compared to various signal compensation techniques requiring the prior measurement of baseline data subject to different circumstances (e.g., different temperatures), the utilization of the damage-associated mode conversion opens a new way to achieve baseline-free damage detection without any prior knowledge of the circumstance. Mode conversion is an intrinsic feature of guided waves occurring due to nonsymmetric thickness variation of structures (Cho and Rose 1996). By recognizing that most damage types can be **equivalently** regarded as certain forms of local reduction of structural thickness, the examination of converted wave modes can be well linked with damage identification. Sohn et al. presented a new approach for damage detection in metal plates using new converted modes associated with nonpenetrative cracks (Kim and Sohn 2007; An and Sohn 2010). More recently, the mode conversion of guided waves in composite plates caused by damage in terms of delamination (Pudipeddi et al. 2019) and fatigue damage accumulation (Zhang et al. 2020a) have also been investigated.

While with potential in baseline-free damage detection, the converted modes are normally concealed in the primitive multimode guided waves and are unable to be utilized directly. Therefore, a vital task is the development of effective strategies for converted mode extraction (CME). Attempts have been made in this field in ways such as excitation control (Giurgiutiu 2005), orthogonality relation (Ratassepp et al. 2015), and two-dimensional fast Fourier transform (Gao et al. 2017). Notably, Zhou et al. (2019) developed a basis mode reconstruction technique for CME, **in which the basis modes are defined as the intrinsic wave modes existing in damage-free structures**. In detail, the basis modes are obtained based on **waveform correlation analysis**, which can largely reduce the complexity of excitation control and signal processing.

**It is reasonable to predict that the advantages of the conventional PDI and the CME methods can be combined to produce accurate damage detection results that are independent of the obtainment of baseline data.** However, to the authors' knowledge, relevant studies are still rare. In this work, a novel baseline-free approach is proposed relying on the integrated utilization of PDI and CME, with a damage diagnostic imaging algorithm derived based on the probability diagnostic and the basis mode reconstruction technique. The effectiveness of the CME-PDI approach is first examined numerically, and an experiment is carried out subsequently by taking into account the effect of temperature variation. Compared with conventional PDI, the CME-PDI approach shows apparently enhanced accuracy and stability in damage localization, which is deemed important in potential applications.

## Methodology

The procedure of the CME-PDI approach is illustrated as a flow diagram in Fig. 1. The approach is mainly formed by two parts, the CME and PDI, which are **elaborated** in the following sections.

### Implementation of CME Based on Wave Reconstruction Technique

During the propagation of guided waves, converted modes are generated resulting from the occurrence of nonsymmetric structural thickness variation that can be well associated with various types of nonpenetrating damages (Cho 2000). The converted modes are usually hidden in primitive multimode guided wave signals containing the basis modes. In this work, CME is carried out according to the basis mode reconstruction technique recently developed by Zhou et al. (2019) based on the signal correlation analysis. The numerical calculation of the basis mode signal in guided wave propagation has been given by Liu and Yuan (2009) based on the dispersion curve and excitation signal. By recognizing that the primitive wave signal is the combination of the basis mode and converted mode signals, the converted mode signals can be simply expressed

$$s_c(r, t) = \tilde{s}(r, t) - s_b(r, t) \quad (1)$$

where  $\tilde{s}(r, t)$  and  $s_b(r, t)$  = primitive and basis mode signal, respectively; and  $r$  and  $t$  = propagation distance and time, respectively. Specifically,  $s_b(r, t)$  can be approximated as the superposition of signals subject to a series of individual modes, expressed

$$s_b(r, t) \approx s(r, t, C_m, t_m) = \sum_m C_m G_m(r, t + t_m) \quad (2)$$

where  $C_m$  and  $t_m$  = amplitude and time delay of the  $m$ th mode, respectively; and  $G_m(r, t)$ , the pure signal of the  $m$ th mode, can be calculated based on the propagation characteristic usually extracted from dispersion curves. The basis mode signals can be reconstructed by adjusting the values of  $C_m$  and  $t_m$  for each mode adaptively according to a correlation analysis of the waveforms, relying on which the converted mode signals can then be obtained according to Eq. (1). As well known, the basis modes are in terms of a variety of S and A modes of guided waves. The converted modes can be separated from the real-time total waveform, leading to

$$\begin{aligned} s_c(r, t) &= \tilde{s}(r, t) - s(r, t, C_m, t_m) \\ &= s(r, t) - C_S G_S(r, t + t_S) - C_A G_A(r, t + t_A) \end{aligned} \quad (3)$$

In applications, the basis modes of ease to be reconstructed and proper for damage diagnostics are normally selected with the assistance of computed dispersion curves, which are introduced as follows.

### Computation of Dispersion Curves

The dispersion curves of wave propagation can be calculated both in analytical and numerical ways (Pavlovic et al. 1997; Han et al. 2009; Baid et al. 2015). In this study, **the dispersion curves of homogeneous plate structures are calculated based on the semianalytical finite-element (SAFE) method** (Yang et al. 2019; Zhang et al. 2020b). The displacement distribution along the wave propagation direction in the plate is assumed to be harmonic, whereas the cross-section of the plate is discretized into a number of finite-elements, as illustrated in Fig. 2(a). Then, the **eigenvalue** equation of the SAFE method is established to be (Zhang et al. 2020c)

分离原理

计算色散曲线的方式有哪些

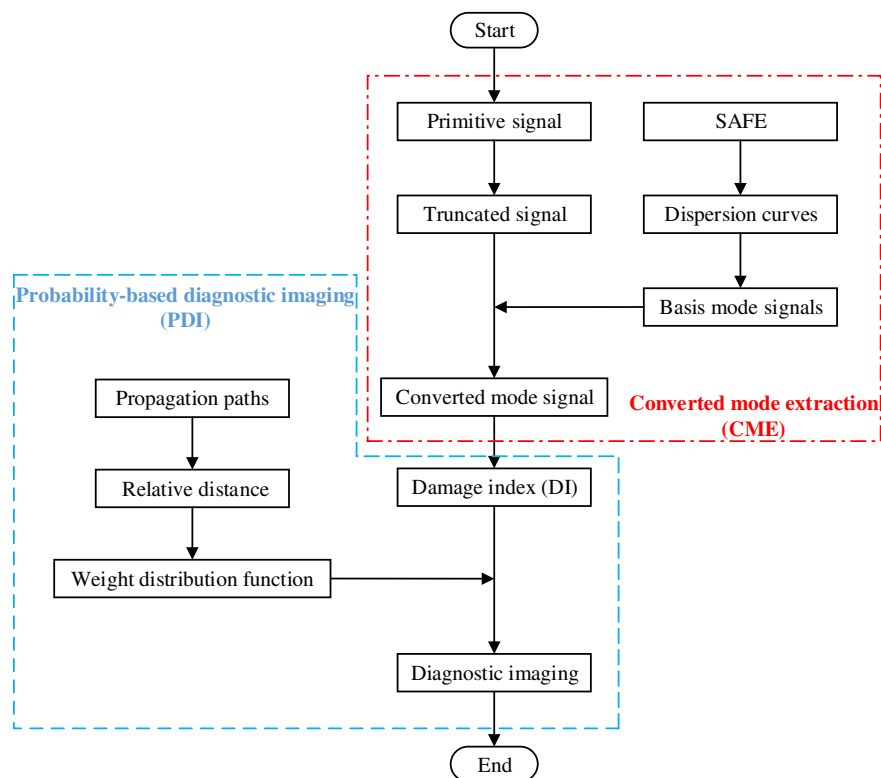


Fig. 1. Flow diagram of CME-PDI.

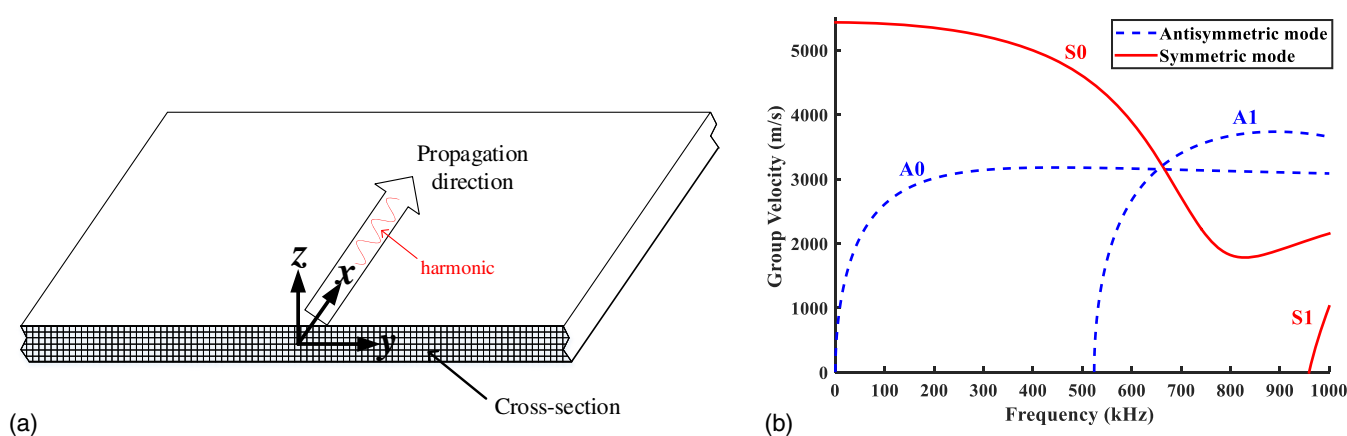


Fig. 2. (a) Schematic of the SAFE model for guided wave propagation in plate-like structures; and (b) dispersion curves of the 3 mm thick aluminum plate.

$$[\mathbf{K}_1 + ik\mathbf{K}_2 + k^2\mathbf{K}_3 - \omega^2\mathbf{M}]_M \mathbf{Q} = 0 \quad (4)$$

$$c_g = \frac{d\omega}{dk} \quad (5)$$

where  $\mathbf{K}_1$ ,  $\mathbf{K}_2$ ,  $\mathbf{K}_3$ , and  $\mathbf{M}$  are matrices associated with the structural geometric and material properties;  $\mathbf{Q}$  = displacement vector; and  $k$  and  $\omega$  = wave number and circular frequency, respectively. Eq. (4) can be solved in several ways (Ahmad 2011), and in this study, we employ an approach to solve the frequency by fixing the wave number due to the less eigenvector. Then, the dispersion curves are obtained according to the formula of the group velocity (Rose 2014)

As an example, the dispersion curves of an aluminum plate were computed. The plate has a thickness of 3 mm, mass density of 2,700 kg/m<sup>3</sup>, Young's modulus of 71 GPa, and Poisson's ratio of 0.33. Fig. 2(b) shows the calculated dispersion curves consisting of group velocities and frequencies. It can be observed that within the frequency range of 200–300 kHz, the wave modes are dominated by S0 and A0, which exhibit a small degree of dispersion and considerable difference in the velocity. Such features make the

frequency range appropriate for CME implementation and damage diagnostics. However, the chosen frequency range varies with the thickness and properties.

### PDI Based on the Converted Modes

In the PDI algorithm, the diagnostic area is divided into meshes for image projection, and the presence of the probability of damage is yielded by summing DIs distributing in elliptical regions associated with different propagation paths (Zhou et al. 2011). Previous studies have used the time-domain energy of scatter signal, which is calculated by subtracting a real-time signal from a baseline signal (Michaels 2008). By integrating the PDI and CME methods, a baseline-free DI is defined in terms of the time-domain energy of the converted modes. For the case only involving S0 and A0 wave modes, the damage index (DI) is expressed as

$$DI = \int_{t_1}^{t_2} s_c^2(t) dt \quad (6)$$

创新：修改DI  
其他公式未动

where  $t_1$  and  $t_2$  = truncation points of a time window, ranging between the peak values of the reconstructed S0 and A0 mode signals, respectively, as shown in Fig. 3.

Subsequently, the probability of damage at a given grid point  $(x, y)$  is given (Wang et al. 2010)

$$P(x, y) = \sum_{i=1}^N DI_i \cdot W_i[R_i(x, y)] \quad (7)$$

where  $DI_i$  is calculated using Eq. (6); and  $W_i[R_i(x, y)]$  = weight distribution function of the  $i$ th path in terms of a nonnegative linear decreasing function with the form of (Wu et al. 2014)

$$W_i[R_i(x, y)] = \begin{cases} 1 - \frac{R_i(x, y)}{\beta}, & R_i(x, y) < \beta \\ 0, & R_i(x, y) \geq \beta \end{cases} \quad (8)$$

which depends on the defined  $R_i(x, y)$ , defined as the relative distance between  $(x, y)$  and the  $i$ th path

$$R_i(x, y) = \frac{d_{e,i}(x, y) + d_{r,i}(x, y) - L_i}{L_i} \quad (9)$$

where  $L_i$  = length of the  $i$ th path;  $d_{e,i}$  = distance between  $(x, y)$  and the exciting transducer;  $d_{r,i}$  = distance between  $(x, y)$  and the receiving transducer; and  $\beta$  = scaling parameter that controls the size of the effective elliptical distribution area (Liu et al. 2016).

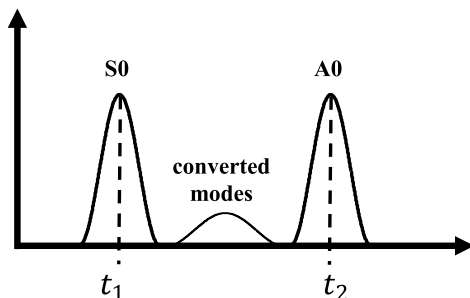


Fig. 3. Modes in the time window.

## Numerical Validation

### FE Modeling

### 有限元仿真

To verify the effectiveness of the proposed CME-PDI approach, the FE simulation is carried out using the software ABAQUS. The models of an aluminum plate and the bonded transducers are built and shown in Fig. 4. Twelve piezoelectric transducers (PZT) are mounted on the surface of the plate to both excite and receive guided waves. The plate is in a square shape with a side length of 450 mm and a thickness of 3 mm. The dimension of the circle-shaped PZT is uniformly  $\phi 8 \times 0.45$  mm. The material properties are the same as those presented in SAFE modeling. To avoid the impact of reflective waves from boundaries, an absorbing region is built around the four edges of the plate using incremental damping absorbing layers (Moreau and Castaings 2008). The size of the element is 1 mm, which can meet the discretized criterion of guided wave modeling (Moser et al. 1999).

A circle shape sensor network with  $5 \times 12$  propagation paths is arranged, as shown in Fig. 5. A single nonpenetrating damaged zone is created in the plate in two independent damage cases, with details listed in Table 1. A 10-cycle sinusoidal toneburst waveform centered at the excitation frequency of 250 kHz is modulated by a

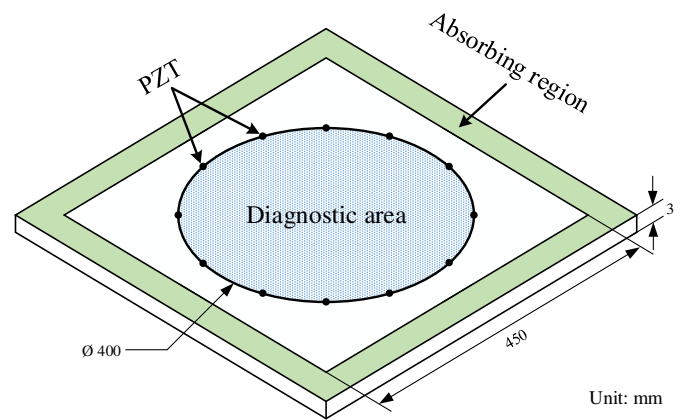


Fig. 4. Schematic of the model of the FE simulation.

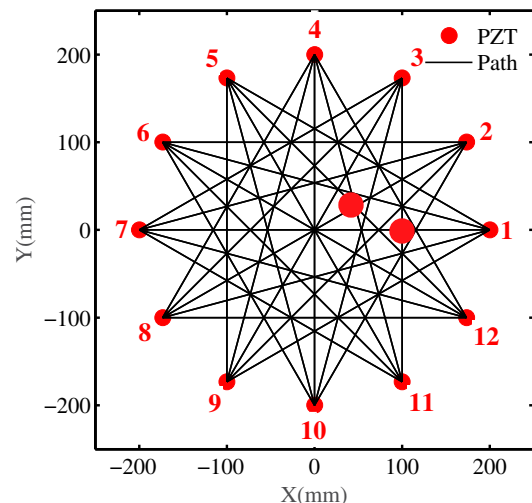
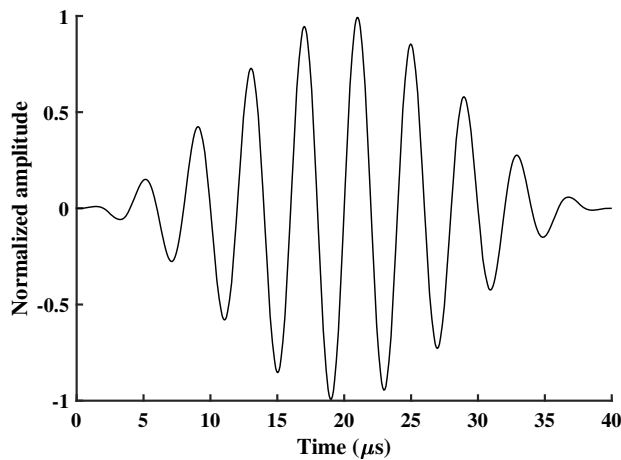


Fig. 5. FE configuration for propagation paths.



**Table 1.** Damage setting

Damage	Size (mm)	Depth (mm)	Location (x, y) (mm)
#1	$\phi 20$	1.5	(100, 0)
#2	$\phi 20$	1.5	(50, 50)

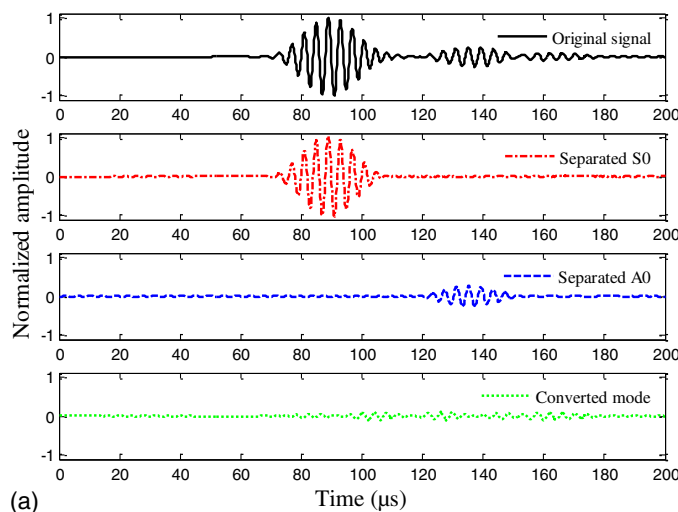
**Fig. 6.** Excitation signal with the excitation frequency of 250 kHz.

Hanning window and then used to excite guided waves. The excitation signal is shown in Fig. 6, and the Hanning window is defined (Oppenheim et al. 1999)

$$w(n) = \frac{1}{2} \left[ 1 - \cos\left(\frac{2\pi(n-1)}{N}\right) \right], \quad 0 \leq n \leq N \quad (10)$$

## Results and Discussions

CME is performed according to Eq. (3). Fig. 7 shows the basis and converted mode signals separated from the primitive multimode guided wave signal along two representative paths, which are labeled by the indices of sensors at the two ends of the paths. It is observed that the magnitude of the converted mode is more



prominent in Fig. 7(b) than Fig. 7(a), owing to that the damage in Case #1 is located along Path 3-11 rather than Path 2-6.

The CMS-PDI approach is then applied, in which the DIs are calculated according to Eq. (6) based on the extracted converted mode signals. To further improve the precision of the damage localization, the DIs are processed by setting

$$DI_i = \begin{cases} DI_i, & DI_i \geq \frac{DI_{\max}}{2} \\ 0, & DI_i < \frac{DI_{\max}}{2} \end{cases} \quad (11)$$

The calculated DIs at different paths are shown in Fig. 8. It can be seen that the paths with the max DI are 3-11 (i.e., Path 15) in Case #1 and 5-12 (i.e., Path 24) in Case #2, which is because the damaged zones are located on these two paths. The diagnostic results are then imaged based on these DIs, as shown in Fig. 9. To estimate the accuracy of the damage localization, the relative error is defined

$$E_r = \frac{E_a}{L_{\min}} \times 100\% \quad (12)$$

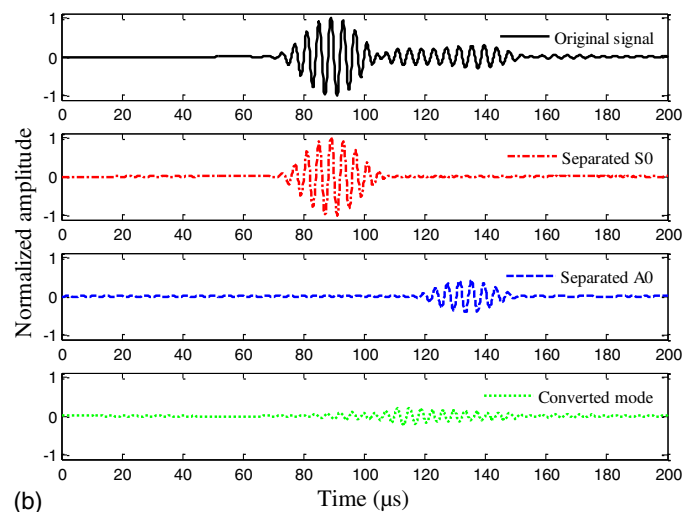
where  $E_a$  = absolute localization error; and  $L_{\min}$  = minimum length of the propagation paths. The damage identification errors are listed in Table 2. It can be seen that the CME-PDI is able to produce high detection accuracy, with location errors smaller than the damage size (i.e., 20 mm).

定位误差跟损伤直径比？

## Experimental Verification

### Comparison of Conventional PDI and CME-PDI Methods Subjected to Temperature Variation

As pointed out, the temperature effect has a significant impact on the damage detection precision of conventional PDI due to the high sensitivity of wave propagation characteristics to temperature variation. The dispersion curves of the plate model under different temperatures are calculated according to the thermoacoustoelastic semianalytical finite-element method (Yang et al. 2020). Fig. 10 presents the distributions of dispersion curves at temperatures varying with a uniform interval of 15°C, and the corresponding guided wave signals at 250 kHz are shown in Fig. 11.

**Fig. 7.** Mode separation of multimode signals in some paths: (a) Path 2-6 on #1; and (b) Path 3-11 on #1.

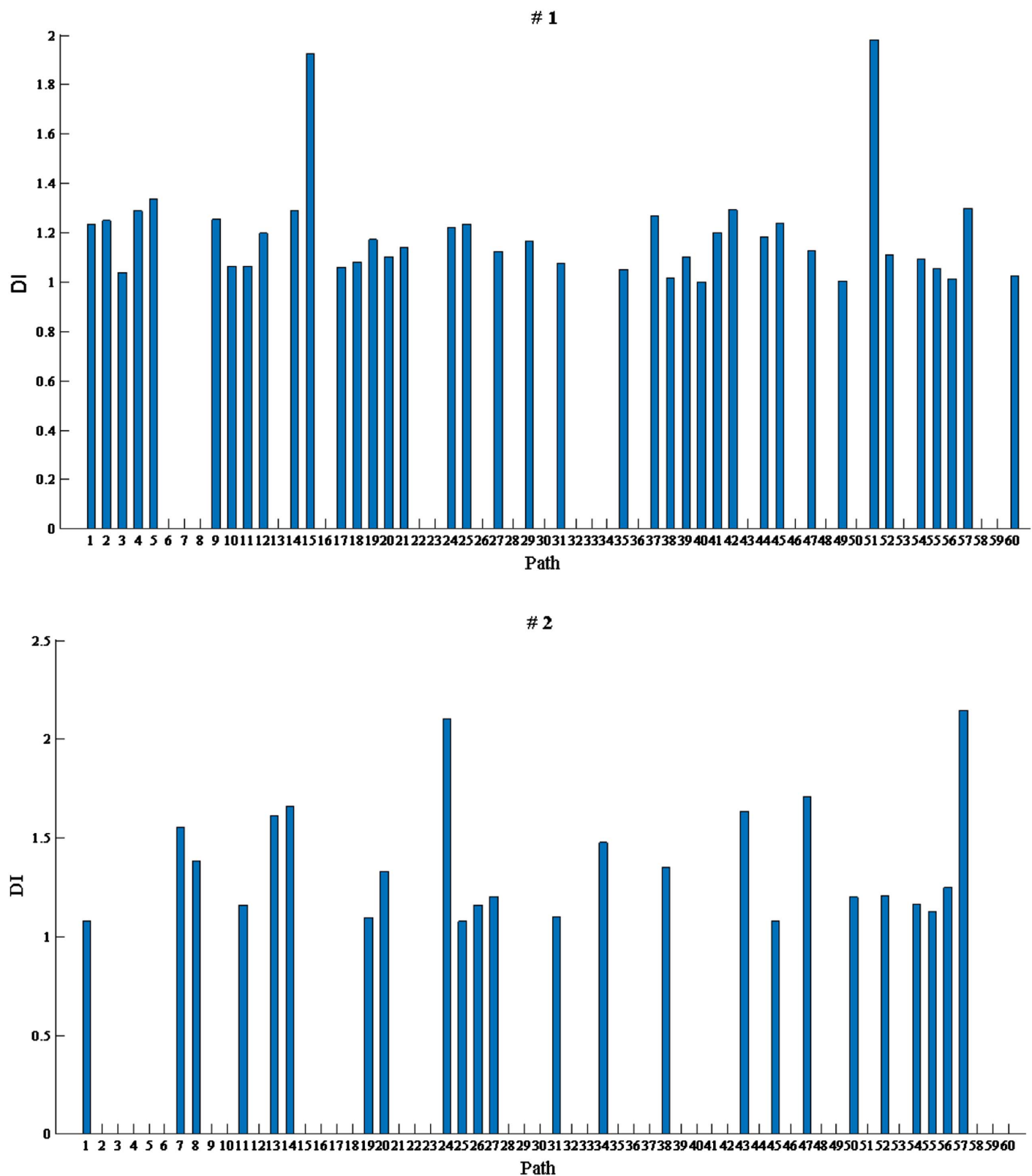


Fig. 8. Damage index.

Basically, the propagation velocity at the given frequency changes along with the temperature linearly. More importantly, the guided waves under different temperatures only exhibit a difference in the phase, which means that the basis modes can be well constructed merely relying on phase-shifting strategy, which can be

realized by the CME technique relying on waveform correlation analysis. In contrast, the temperature variation will cause deviation between the real-time and baseline signals obtained under a constant temperature, resulting in false alarms of damage when using the conventional PDI method. The damage detection accuracy of

传统方法受温度影响  
产生信号偏移致报假  
警

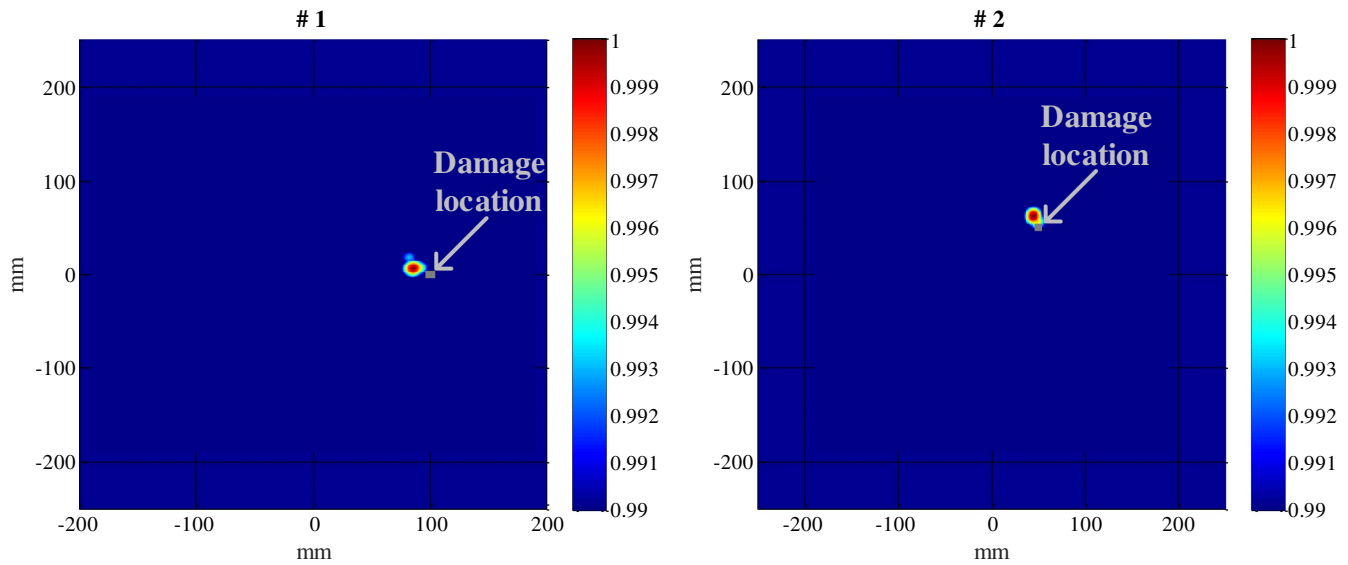


Fig. 9. Diagnostic images of FE using MS-PDI.

Table 2. FE damage diagnostic locations 绝对误差

Damage	Location (x, y) (mm)	$E_a$ (mm)	$E_r$ (%)
#1	(85, 7)	16.55	4.78
#2	(44, 63)	14.32	4.13

the conventional PDI and CME-PDI methods are compared experimentally in the following section.

Fig. 12 shows the experimental setup for damage diagnosis in an aluminum plate. The PZT sensors are mounted on the surface of the aluminum plate with the layout the same as that in the FE model. The  $3 \times 12$  propagation paths are applied as shown in Fig. 13. The number of paths in the experiment is smaller than in the preceding simulation because several paths close to the boundaries are not included to prevent the impact of the reflected waves. An integrated guided wave-based SHM system, with self-developed hardware and software, is developed to excite and capture guided wave signals at a sampling rate of 12 MHz. A 10-cycle sinusoidal toneburst

waveform modulated by a Hanning window is generated, with the excitation frequency centered at 200 kHz.

A temperature control system integrated by a resistive heater and automatic temperature regulation hardware is applied to provide a temperature higher than room temperature, whereas liquid nitrogen is used to provide a low-temperature environment. Temperature error is controlled at  $0.2^\circ\text{C}$ . Damage diagnosis is performed at four different temperatures, i.e.,  $-5^\circ\text{C}$ ,  $10^\circ\text{C}$ ,  $25^\circ\text{C}$ , and  $40^\circ\text{C}$ . And a thermocouple thermometer is used to monitor the temperature of the plate in real-time. For the implementation of the conventional baseline-dependent PDI method, guided wave signals under the pristine condition of the plate are collected at  $25^\circ\text{C}$  to be used as the baseline data. Damage with a size of  $\phi 20 \times 1.5$  mm is then created on the plate surface at the location of (50, 50 mm).

Damage localization results based on the conventional PDI and CME-PDI methods are both listed in Table 3, and the corresponding diagnostic images are shown in Figs. 14 and 15, respectively. According to Figs. 14(c) and 15(c), it can be seen that both the conventional PDI and CME-PDI methods are able to achieve satisfactory diagnostic accuracy at a temperature of  $25^\circ\text{C}$ , with distance

### 自主研发

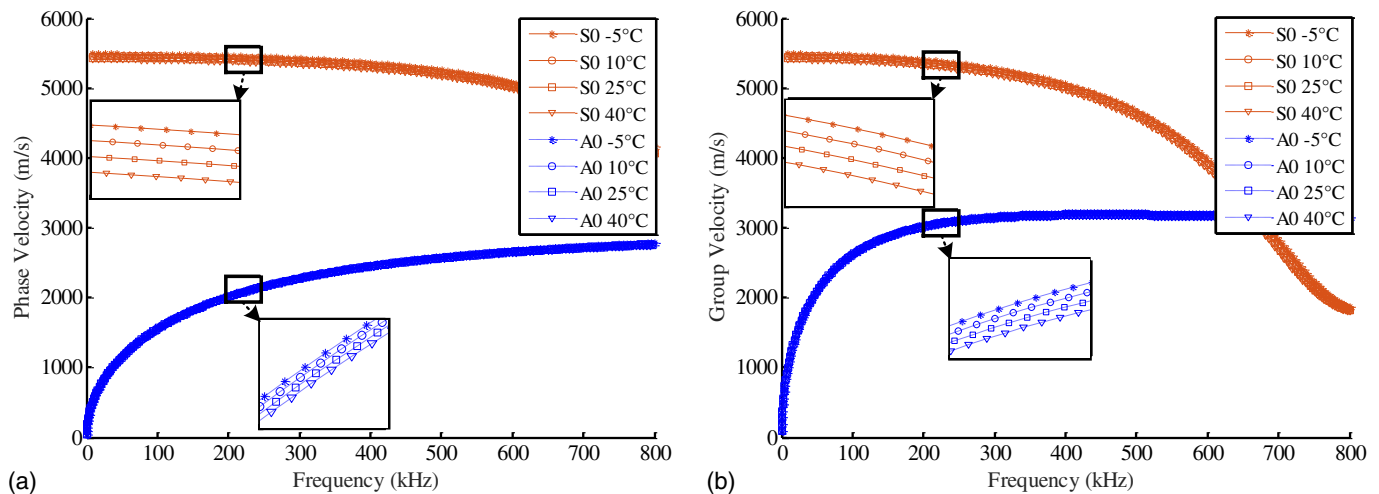
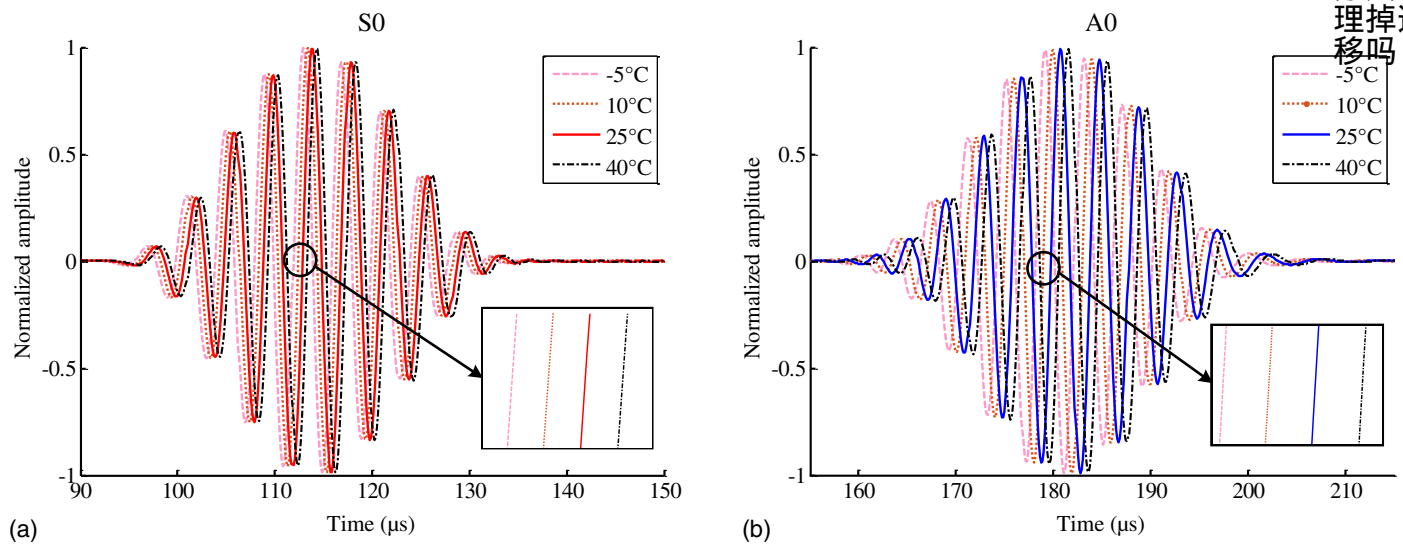
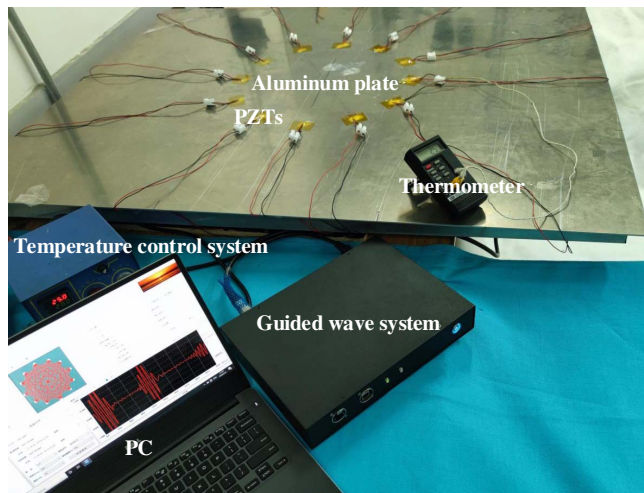


Fig. 10. Dispersion curves at  $-5^\circ\text{C}$ ,  $10^\circ\text{C}$ ,  $25^\circ\text{C}$ , and  $40^\circ\text{C}$ : (a) phase velocities curves; and (b) group velocities curves.



**Fig. 11.** Guide waves propagating 0.5 m at  $-5^{\circ}\text{C}$ ,  $10^{\circ}\text{C}$ ,  $25^{\circ}\text{C}$ , and  $40^{\circ}\text{C}$ : (a) S0 mode; and (b) A0 mode.



**Fig. 12.** Photograph of the experimental setup.

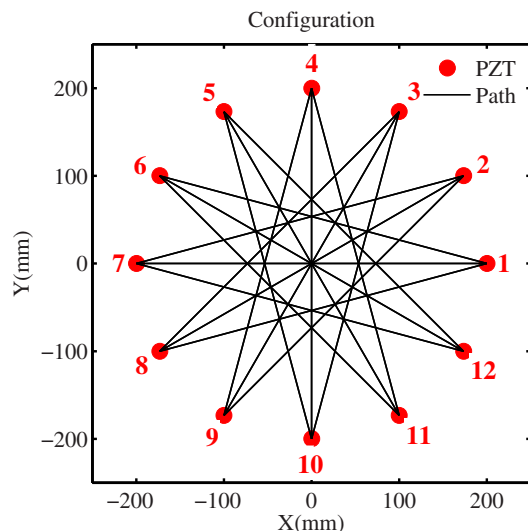


**Fig. 13.** Experimental configuration for propagation paths.

**Table 3.** Damage localization results under varying environments

Temperature ( $^{\circ}\text{C}$ )	Conventional PDI location (mm) and $E_r$	CME-PDI location (mm) and $E_r$
-5	(-17, -60) 33.34%	(44, 44) 2.20%
10	(0, 0) 18.30%	(43, 44) 2.39%
25	(46, 43) 2.09%	(42, 41) 3.12%
40	(44, -44) 24.38%	(41, 41) 3.29%

(50,50)损伤

errors comparable to the damage size. However, Figs. 14(a, b, and d) show that the detection errors of the conventional PDI increase drastically at temperatures other than  $25^{\circ}\text{C}$  due to the fact that baseline data is influenced greatly by temperature variation. On the contrary, the CME-PDI approach shows remarkable immunity to temperature influence by seeing that the errors of damage localization remain considerably low in Figs. 15(a, b, and d). The relative distance errors of the conventional PDI and CME-PDI are specified in Table 3 from which the much-enhanced environmental adaptability of the CME-PDI approach can be clearly observed.

### Noise Effect on the CME-PDI Method

Studies on noise sensitivity of the proposed CME-PDI method are conducted in this section. The collected guided wave signals are superimposed with artificial white Gaussian noise, which is generated from a random Gaussian process with zero mean. The signal-to-noise ratio (SNR) is used to control the noise level expressed

$$\text{SNR} = 10 \log_{10} \left( \frac{\text{ENG}(\text{signal})}{\text{ENG}(\text{noise})} \right) \quad (13)$$

where  $\text{ENG}(\text{noise})$  and  $\text{ENG}(\text{signal})$  = time-domain energy of noise and the original signal without noise interference, respectively. As a result, smaller SNR values are in accordance with larger noise levels.

The CME-PDI algorithm is then applied using noise-contaminated signals with SNRs of 13 dB, 12 dB, and 10 dB, respectively, at  $25^{\circ}\text{C}$ . At each SNR value, the additions of random white Gaussian noise are repeated 20 times, among which the detection results with the maximum errors are considered. The diagnostic images are shown in Fig. 16. It can be seen that the location



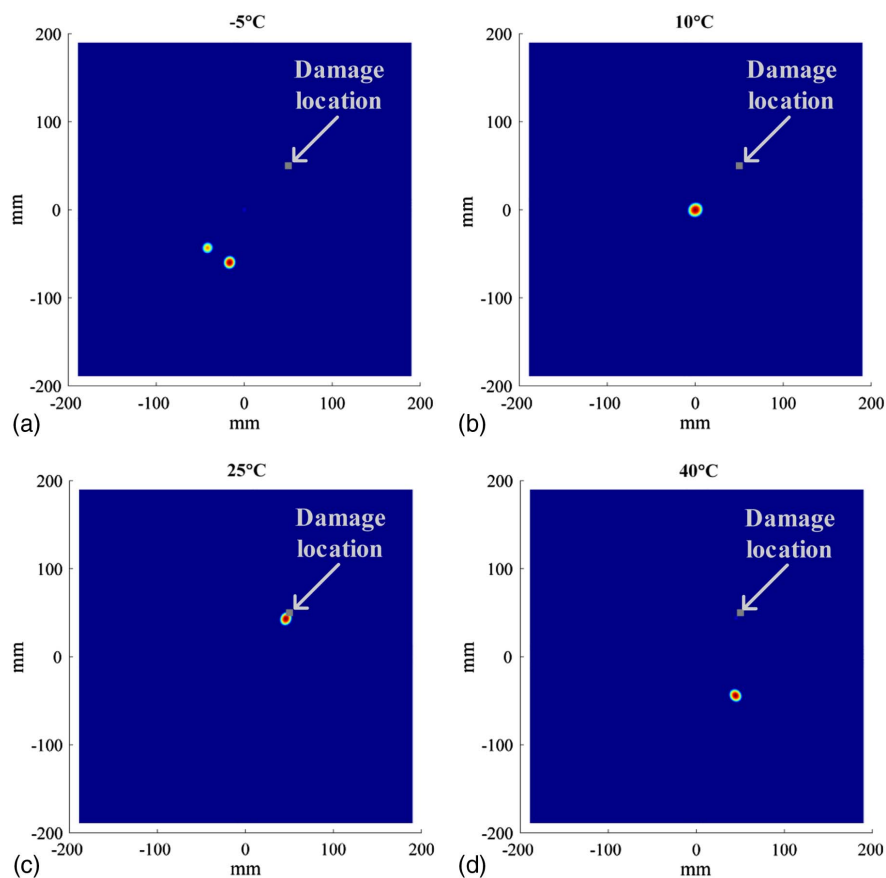


**Fig. 14.** Conventional PDI at (a)  $-5^{\circ}\text{C}$ ; (b)  $10^{\circ}\text{C}$ ; (c)  $25^{\circ}\text{C}$ ; and (d)  $40^{\circ}\text{C}$ .

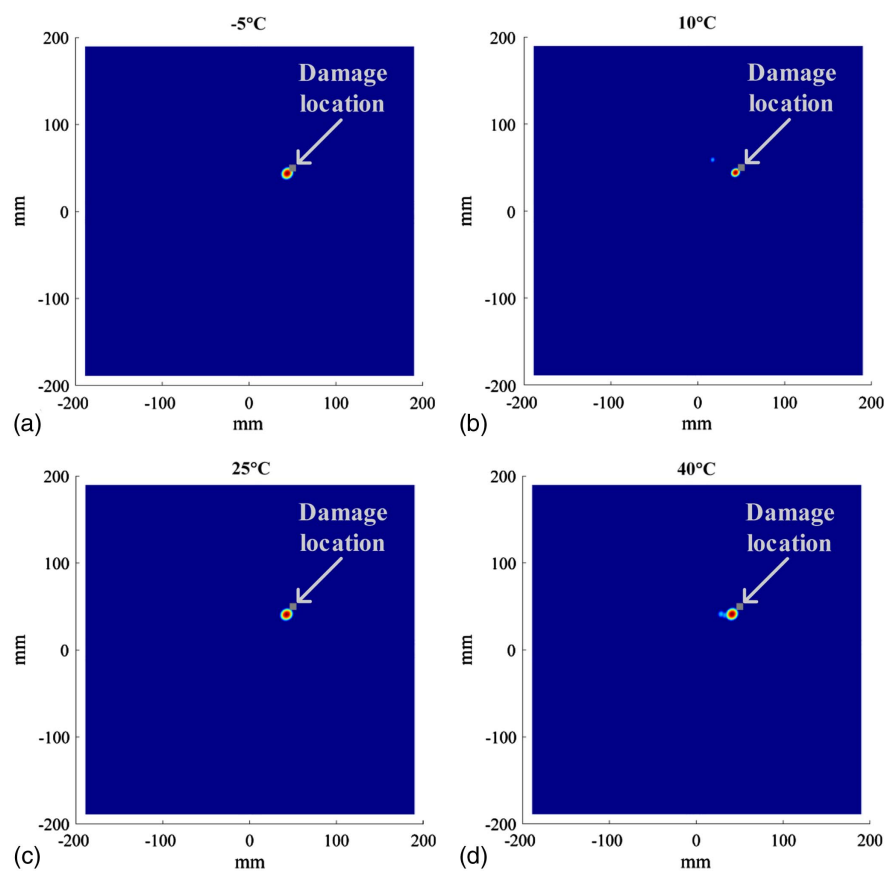


**Fig. 15.** CME-PDI at (a)  $-5^{\circ}\text{C}$ ; (b)  $10^{\circ}\text{C}$ ; (c)  $25^{\circ}\text{C}$ ; and (d)  $40^{\circ}\text{C}$ .

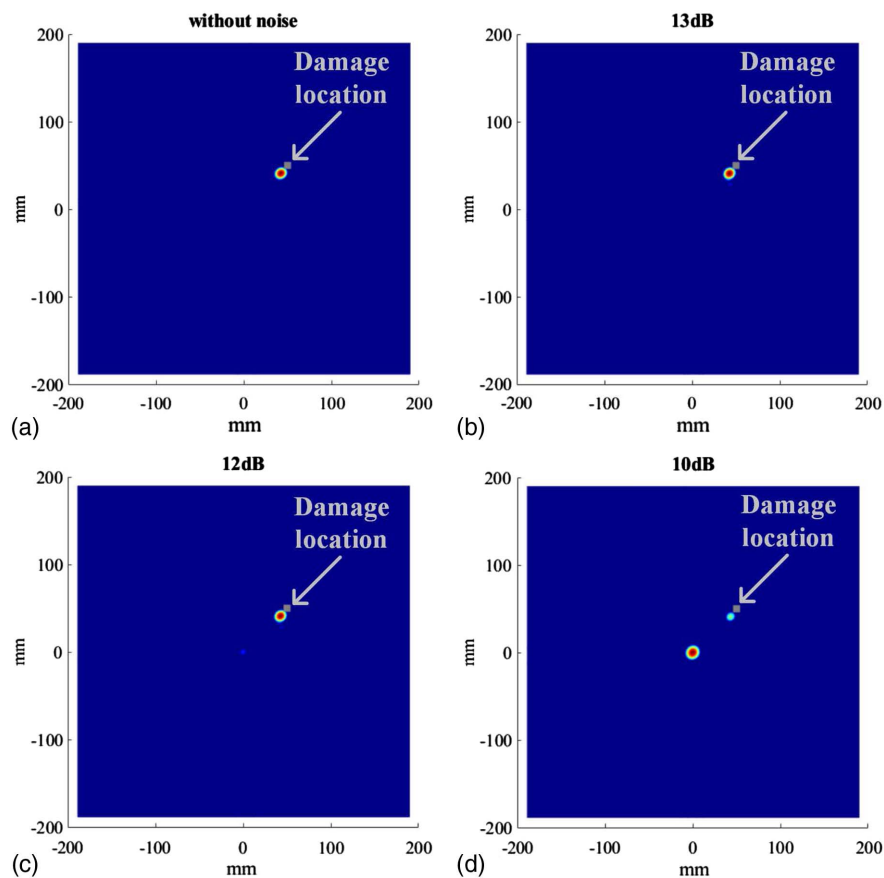


Fig. 16. CME-PDI at different SNRs: (a) without noise; (b) 13 dB; (c) 12 dB; and (d) 10 dB.

detection errors under an SNR of 13 and 12 dB are 3.16% and 3.12%, respectively, which is highly consistent with the detection results using noise-free signals. However, the detection error under the SNR of 10dB reaches a relatively large level, around 18.30%. In general, the CME-PDI method shows satisfactory noise robustness, and damage can be well-identified when the noise energy is lower than one-tenth of the energy of the original guided wave signal, according to Eq. (13).

## Conclusions

This paper proposes a modified damage diagnostic imaging approach featured by the independence of a prior measurement of baseline data of guided wave signals. The approach is developed by integrating the probability-based diagnostic imaging (PDI) method with a converted mode extraction (CME) technique relying on basis mode reconstruction, in which the basis modes are selected with the assistance of dispersion curves calculated using the SAFE method. Time-domain energy of the converted modes is utilized to construct the DI of the approach for probability-based diagnostic imaging. According to the numerical and experimental results, it is shown that the converted modes can be successfully extracted and applied for damage diagnostic imaging. More importantly, the CME-PDI approach shows superior accuracy and immunity to environmental factors (i.e., temperature) compared to the conventional baseline-dependent PDI method. Such an advantage is of vital importance for SHM in real applications. In addition, the SNR threshold is 10 dB.

The proposed CME-PDI approach is suitable for single damage in this study, so the diagnosis of multiple damages will be investigated in our future work. In addition, the effectiveness of the CME-PDI approach is worthy of being examined by taking into account factors including more complex structures (e.g., composite laminates and multilayered structures), the influence of more environmental factors (e.g., loading conditions), and so forth.

## Data Availability Statement

All data, models, and code generated or used during the study appear in the published article.

## Acknowledgments

This work was supported by the National Key Research and Development Program of China (Grant No. 2018YFA0702800), the National Natural Science Foundation of China (Grant Nos. 12072056, 51805068, and 11702051), and the Fundamental Research Funds for the Central Universities (DUT19ZD101).

## References

- Ahmad, Z. A. B. 2011. "Numerical simulations of lamb waves in plates using a semi-analytical finite element method." Ph.D. thesis, Institute of Mechanics, Otto von Guericke Univ. Magdeburg.

- Alem, B., A. Abedian, and K. Nasrollahi-Nasab. 2016. "Reference-free damage identification in plate-like structures using lamb-wave propagation with embedded piezoelectric sensors." *J. Aerosp. Eng.* 29 (6): 04016062. [https://doi.org/10.1061/\(ASCE\)AS.1943-5525.0000646](https://doi.org/10.1061/(ASCE)AS.1943-5525.0000646).
- An, Y.-K., and H. Sohn. 2010. "Instantaneous crack detection under varying temperature and static loading conditions." *Struct. Control Health Monit.* 17 (7): 730–741. <https://doi.org/10.1002/stc.394>.
- Baid, H., C. Schaal, H. Samajder, and A. Mal. 2015. "Dispersion of lamb waves in a honeycomb composite sandwich panel." *Ultrasonics* 56 (Feb): 409–416. <https://doi.org/10.1016/j.ultras.2014.09.007>.
- Bhalla, S., and C. Soh. 2004. "Structural health monitoring by piezo-impedance transducers. II: Applications." *J. Aerosp. Eng.* 17 (4): 166–175. [https://doi.org/10.1061/\(ASCE\)0893-1321\(2004\)17:4\(166\)](https://doi.org/10.1061/(ASCE)0893-1321(2004)17:4(166)).
- Borate, P., G. Wang, and Y. Wang. 2020. "Data-driven structural health monitoring approach using guided lamb wave responses." *J. Aerosp. Eng.* 33 (4): 04020033. [https://doi.org/10.1061/\(ASCE\)AS.1943-5525.0001145](https://doi.org/10.1061/(ASCE)AS.1943-5525.0001145).
- Cho, Y. 2000. "Estimation of ultrasonic guided wave mode conversion in a plate with thickness variation." *IEEE Trans. Ultrason. Ferroelectr. Freq. Control* 47 (3): 591–603. <https://doi.org/10.1109/58.842046>.
- Cho, Y., and J. L. Rose. 1996. "A boundary element solution for a mode conversion study on the edge reflection of lamb waves." *J. Acoust. Soc. Am.* 99 (4): 2097–2109. <https://doi.org/10.1121/1.415396>.
- Fan, Z., A. F. Mark, M. J. S. Lowe, and P. J. Withers. 2015. "Nonintrusive estimation of anisotropic stiffness maps of heterogeneous steel welds for the improvement of ultrasonic array inspection." *IEEE Trans. Ultrason. Ferroelectr. Freq. Control* 62 (8): 1530–1543. <https://doi.org/10.1109/TUFFC.2015.007018>.
- Gao, D., Z. Wu, L. Yang, and Y. Zheng. 2016. "Guide waves-based multi-damage identification using a local probability-based diagnostic imaging method." *Smart Mater. Struct.* 25 (4): 045009. <https://doi.org/10.1088/0964-1726/25/4/045009>.
- Gao, F., L. Zeng, J. Lin, and Z. Luo. 2017. "Mode separation in frequency-wavenumber domain through compressed sensing of far-field lamb waves." *Meas. Sci. Technol.* 28 (7): 075004. <https://doi.org/10.1088/1361-6501/aa6c54>.
- Giurgiutiu, V. 2005. "Tuned lamb wave excitation and detection with piezoelectric wafer active sensors for structural health monitoring." *J. Intell. Mater. Syst. Struct.* 16 (4): 291–305. <https://doi.org/10.1177/1045389X05050106>.
- Gorgin, R., Y. Luo, and Z. Wu. 2020. "Environmental and operational conditions effects on lamb wave based structural health monitoring systems: A review." *Ultrasonics* 105 (Jul): 106114. <https://doi.org/10.1016/j.ultras.2020.106114>.
- Han, S., A. N. Palazotto, and C. L. Leakeas. 2009. "Finite-element analysis of lamb wave propagation in a thin aluminum plate." *J. Aerosp. Eng.* 22 (2): 185–197. [https://doi.org/10.1061/\(ASCE\)0893-1321\(2009\)22:2\(185\)](https://doi.org/10.1061/(ASCE)0893-1321(2009)22:2(185)).
- Kannusamy, M., S. Kapuria, and S. Sasmal. 2020. "Accurate baseline-free damage localization in plates using refined lamb wave time-reversal method." *Smart Mater. Struct.* 29 (5): 055044. <https://doi.org/10.1088/1361-665X/ab8028>.
- Kim, S. B., and H. Sohn. 2007. "Instantaneous reference-free crack detection based on polarization characteristics of piezoelectric materials." *Smart Mater. Struct.* 16 (6): 2375–2387. <https://doi.org/10.1088/0964-1726/16/6/042>.
- Liu, K., S. Ma, Z. Wu, Y. Zheng, X. Qu, Y. Wang, and W. Wu. 2016. "A novel probability-based diagnostic imaging with weight compensation for damage localization using guided waves." *Struct. Health Monit.* 15 (2): 162–173. <https://doi.org/10.1177/1475921715627491>.
- Liu, L., and F. G. Yuan. 2009. "A linear mapping technique for dispersion removal of lamb waves." *Struct. Health Monit.* 9 (1): 75–86. <https://doi.org/10.1177/1475921709341012>.
- Michaels, J. E. 2008. "Detection, localization and characterization of damage in plates with an in situ array of spatially distributed ultrasonic sensors." *Smart Mater. Struct.* 17 (3): 035035. <https://doi.org/10.1088/0964-1726/17/3/035035>.
- Moreau, L., and M. Castaings. 2008. "The use of an orthogonality relation for reducing the size of finite element models for 3D guided waves scattering problems." *Ultrasonics* 48 (5): 357–366. <https://doi.org/10.1016/j.ultras.2008.01.005>.
- Moser, F., L. J. Jacobs, and J. Qu. 1999. "Modeling elastic wave propagation in waveguides with the finite element method." *NDT E Int.* 32 (4): 225–234. [https://doi.org/10.1016/S0963-8695\(98\)00045-0](https://doi.org/10.1016/S0963-8695(98)00045-0).
- Oppenheim, A. V., R. W. Schaffer, and R. J. Buck. 1999. *Discrete-time signal processing*. Upper Saddle River, NJ: Prentice Hall.
- Pavlakovic, B., M. Lowe, D. Alleyne, and P. Cawley. 1997. *Disperse: A general purpose program for creating dispersion curves, in review of progress in quantitative nondestructive evaluation: Volume 16A*. Boston: Springer.
- Pudipeddi, G. T., C.-T. Ng, and A. Kotousov. 2019. "Mode conversion and scattering of lamb waves at delaminations in composite laminates." *J. Aerosp. Eng.* 32 (5): 04019067. [https://doi.org/10.1061/\(ASCE\)AS.1943-5525.0001060](https://doi.org/10.1061/(ASCE)AS.1943-5525.0001060).
- Qing, X., S. Beard, A. Kumar, and R. Hannum. 2006a. "A real-time active smart patch system for monitoring the integrity of bonded repair on an aircraft structure." *Smart Mater. Struct.* 15 (3): N66–N73. <https://doi.org/10.1088/0964-1726/15/3/N03>.
- Qing, X., S. J. Beard, A. Kumar, T. K. Ooi, and F. Chang. 2007. "Built-in sensor network for structural health monitoring of composite structure." *J. Intell. Mater. Syst. Struct.* 18 (1): 39–49. <https://doi.org/10.1177/1045389X06064353>.
- Qing, X., H. Chan, S. Beard, and A. Kumar. 2006b. "An active diagnostic system for structural health monitoring of rocket engines." *J. Intell. Mater. Syst. Struct.* 17 (7): 619–628. <https://doi.org/10.1177/1045389X06059956>.
- Qing, X., W. Li, Y. Wang, and H. Sun. 2019. "Piezoelectric transducer-based structural health monitoring for aircraft applications." *Sensors* 19 (3): 545. <https://doi.org/10.3390/s19030545>.
- Ratassep, M., A. Klauson, F. Chati, F. Leon, D. Decultot, G. Maze, and M. Fritzsche. 2015. "Application of orthogonality-relation for the separation of lamb modes at a plate edge: Numerical and experimental predictions." *Ultrasonics* 57 (Mar): 90–95. <https://doi.org/10.1016/j.ultras.2014.10.022>.
- Rose, J. 2014. *Ultrasonic guided waves in solid media: Plates*. Cambridge, UK: Cambridge university press.
- Sohn, H., H. Park, K. Law, and C. Farrar. 2007. "Damage detection in composite plates by using an enhanced time reversal method." *J. Aerosp. Eng.* 20 (3): 141–151. [https://doi.org/10.1061/\(ASCE\)0893-1321\(2007\)20:3\(141\)](https://doi.org/10.1061/(ASCE)0893-1321(2007)20:3(141)).
- Su, Z., L. Ye, and Y. Lu. 2006. "Guided lamb waves for identification of damage in composite structures: A review." *J. Sound Vib.* 295 (3): 753–780. <https://doi.org/10.1016/j.jsv.2006.01.020>.
- Sun, H., A. Zhang, Y. Wang, and X. Qing. 2019. "Baseline-free damage imaging for metal and composite plate-type structures based on similar paths." *Int. J. Distrib. Sens. Networks* 15 (4): 1550147. <https://doi.org/10.1177/1550147719843054>.
- Wang, D., L. Ye, Z. Su, Y. Lu, F. Li, and G. Meng. 2010. "Probabilistic damage identification based on correlation analysis using guided wave signals in aluminum plates." *Struct. Health Monit.* 9 (2): 133–144. <https://doi.org/10.1177/1475921709352145>.
- Wang, Y., L. Gao, S. Yuan, L. Qiu, and X. Qing. 2014. "An adaptive filter-based temperature compensation technique for structural health monitoring." *J. Intell. Mater. Syst. Struct.* 25 (17): 2187–2198. <https://doi.org/10.1177/1045389X13519001>.
- Wang, Y., G. Wang, D. Wu, Y. Wang, B. Miao, H. Sun, and X. Qing. 2020. "An improved matching pursuit-based temperature and load compensation method for ultrasonic guided wave signals." *IEEE Access* 8: 67530–67541. <https://doi.org/10.1109/ACCESS.2020.2985748>.
- Wu, Z., K. Liu, Y. Wang, and Y. Zheng. 2014. "Validation and evaluation of damage identification using probability-based diagnostic imaging on a stiffened composite panel." *J. Intell. Mater. Syst. Struct.* 26 (16): 2181–2195. <https://doi.org/10.1177/1045389X14549873>.
- Xu, H., Z. Zeng, Z. Wu, L. Zhou, Z. Su, Y. Liao, and M. Liu. 2017. "Broadband dynamic responses of flexible carbon black/poly (vinylidene fluoride) nanocomposites: A sensitivity study." *Compos. Sci. Technol.* 149 (Sep): 246–253. <https://doi.org/10.1016/j.compscitech.2017.06.010>.

- Yang, Z., K. Liu, K. Zhou, Y. Liang, J. Zhang, Y. Zheng, D. Gao, S. Ma, and Z. Wu. 2020. "Investigation of thermo-acoustoelastic guided waves by semi-analytical finite element method." *Ultrasonics* 106 (Aug): 106141. <https://doi.org/10.1016/j.ultras.2020.106141>.
- Yang, Z., Z. Wu, J. Zhang, K. Liu, Y. Jiang, and K. Zhou. 2019. "Acoustoelastic guided wave propagation in axial stressed arbitrary cross-section." *Smart Mater. Struct.* 28 (4): 045013. <https://doi.org/10.1088/1361-665X/aadb6e>.
- Yu, X., Z. Fan, M. Castaings, and C. Biateau. 2017. "Feature guided wave inspection of bond line defects between a stiffener and a composite plate." *NDT E Int.* 89 (Jul): 44–55. <https://doi.org/10.1016/j.ndteint.2017.03.008>.
- Zhang, C., Z. Zhang, H. Ji, J. Qiu, and C. Tao. 2020a. "Mode conversion behavior of guided wave in glass fiber reinforced polymer with fatigue damage accumulation." *Compos. Sci. Technol.* 192 (May): 108073. <https://doi.org/10.1016/j.compscitech.2020.108073>.
- Zhang, J., Z. Wu, Z. Yang, C. Gao, K. Liu, Y. Zheng, and K. Zhou. 2020b. "Multimode guided waves-based structural defect localization longitudinally and cross-sectionally in t-bars." *J. Aerosp. Eng.* 33 (4): 04020017. [https://doi.org/10.1061/\(ASCE\)AS.1943-5525.0001134](https://doi.org/10.1061/(ASCE)AS.1943-5525.0001134).
- Zhang, J., Z. Wu, Z. Yang, K. Liu, K. Zhou, and Y. Zheng. 2020c. "Excitation of guided wave modes in arbitrary cross-section structures by applied surface tractions." *Smart Mater. Struct.* 29 (6): 065010. <https://doi.org/10.1088/1361-665X/ab85a1>.
- Zhou, C., Z. Su, and L. Cheng. 2011. "Probability-based diagnostic imaging using hybrid features extracted from ultrasonic lamb wave signals." *Smart Mater. Struct.* 20 (12): 125005. <https://doi.org/10.1088/0964-1726/20/12/125005>.
- Zhou, K., Y. Zheng, J. Zhang, X. Xu, S. Ma, and Z. Wu. 2019. "A reconstruction-based mode separation method of lamb wave for damage detection in plate structures." *Smart Mater. Struct.* 28 (3): 035033. <https://doi.org/10.1088/1361-665X/ab0299>.